Research article

Analysis of structural stability of Ar ion-implanted Pd/Zr/Pd/Ti/Pd multilayer stack in hydrogen annealing environment

C.T. Thethwayo [a,*], C.B. Mtshali [b], Z.M. Khumalo [b], K. Segola [b,d], S. Nsengiyumva [c], N. Mongwaketsi [b], C.L. Ndlangamandla [a], P.N. Biyela [a]

[a] Department of Physics, University of Zululand, Private Bag X1001, KwaDlangezwa, 3886, South Africa
[b] Tandetron Laboratory, IThemba LABS, National Research Foundation, P.O. Box 722, Somerset West, 7129, South Africa
[c] Department of Physics and Electronics, Rhodes University, Grahamstown, 6140, South Africa
[d] Department of Physics, Tshwane University of Technology, Private X680, Pretoria, 001, South Africa

ARTICLE INFO

ABSTRACT

The influence of 150 keV argon ions at fluences in the range of 1×10^{12}–1×10^{16} ions/cm^2 on the stability of the multilayer stack Pd/Zr/Pd/Ti/Pd thin films system, deposited on Ti and Ti$_6$Al$_4$V substrates, under thermal annealing in an H$_2$ environment was investigated. For samples deposited on Ti substrate, RBS revealed structural instability that increases with fluence. This is evidenced by a decrease in the intensity of layers accompanied by increased consumption of the Pd layers. This effect led to the initial individual layers becoming one compound layer and the formation of a new Ti–O–Pd layer, indicating a complete intermixing of layers at 1×10^{16} ions/cm^2. However, for the samples deposited on Ti$_6$Al$_4$V substrate, the Pd layers could still be identified and resolved, indicating an incomplete intermixing of layers. XRD revealed the structural transformation of layers via an intermixing process resulting in the formation of two new phases, TiH$_2$ and ZrH$_2$, classified as face-centered tetragonal (FCT) crystal structures. ERDA confirmed the presence of hydrides in the system indicating the absorption of H into the system to a maximum H amount of ~5.2 at.%, at higher fluence, for the same multilayer stack deposited on both substrates.

1. Introduction

The stability of thin films and compound formation with their associated applications have been the subject of intense research for decades. Factors such as temperature, pressure, and ion irradiation play a major role in the performance of devices associated with such films and compounds [1–6]. For instance, properties of materials elements such as palladium (Pd), titanium (Ti), and zirconium (Zr) in thin film form, can be tailored to a particular application by subjecting them to these conditions [4–8]. These properties have a significant impact on hydrogen storage materials [4], shape-memory alloys (SMAs) [5–7], biomaterials [8], solar cell applications [1, 2], and gas sensing. Our previous study examined the interfacial reaction and phase formation in the Pd/ZrO/Pd/TiO/Pd multilayer stack on the silicon substrate using ion beam techniques [9]. The impact of temperature ramping rate on the phase formation and their activation energies was reported. The results showed that the multilayer stack was stable up to ~370 °C and the inter-diffusion of Pd from both the third and the fifth layer, towards the fourth layer comprising of Ti and O in 2:1 ratio, was observed. In the current

---

investigation, we have introduced ion implantation on Pd/Zr/Pd/Ti/Pd multilayer stack film deposited on Ti and Ti$_6$Al$_4$V as substrates, and gas annealing environment as impactful factors in monitoring the properties of our previously studied system in Ref. [9].

When it comes to hydrogen storage materials, incorporating metals such as palladium (Pd) and titanium (Ti) with other high hydrogen capacity hydrides (such as Mg, Al, Zr, V, NH$_3$, LiNH$_2$, etc.) changes hydrogen uptake/release at lower temperatures [10,11]. Vaidynathan et al. [12] studied 2D polyaramids and found that adding Ti and Zr to them makes them much better at hydrogen absorption. This means that they can be used for onboard and reversible hydrogen storage, especially in light-duty vehicles. Ge et al. [13] confirmed that the addition of Zr results in the formation of small-sized, electron-rich palladium nanoparticles, and that the order in which Zr was added affected the catalytic activity of palladium, thus improving hydrogen absorption. The Pd layer serves as a protective layer to prevent the formation of the oxide layer and to enable the surface dissociation of hydrogen molecules [14–16]. Furthermore, the multilayer stack films create percolative composites due to the interdiffusion of atoms, which could potentially be used in electromagnetic composite applications [17–20]. Percolative composites are binary or multi-component systems. When the content of functional fillers exceeds a particular value (percolative threshold), the dielectric constant of percolative composites will change from positive to negative [19]. The composite systems with properties not dominated by the individual atoms only but by the properties of larger, artificially produced structures are referred to as metamaterials. Fan et al. [20] examined the dielectric characteristics of percolative copper/rutile ceramic composites and discovered that dielectric permittivity depended on the concentration of copper in the composites. This demonstrates that the physical and chemical properties of composites are determined by the experimental method, material type, and concentrations used in their fabrication; thus, the properties of Pd/Zr/Pd/Ti/Pd will be dictated by stacking. Furthermore, doping was also identified as a component that affects the composite properties [21].

Ion implantation and ion mixing have also been reported to positively impact the initial surface activation properties of metals and metal alloys, as well as create crystal defects, which result in improved hydrogen absorption [22–25]. The technique known as 'ion implantation' involves accelerating energetic ions (>10 keV) toward the solid target material surface to introduce dopants and change the material characteristics at low temperatures while being kept in a vacuum. In semiconductor device fabrication, metal finishing, and materials science research, ion implantation is frequently used to improve surface activation properties [26]. The sample surfaces were injected with 150 keV argon ion implantation at fluences ranging from 1×10^{12}–1×10^{16} ion/cm^2 at room temperature to induce ion tracks and assist in enhancing H diffusion onto the system. In this study, argon ion implantation is expected to remove surface film contaminants, induce lattice flaws, and add solute atoms at non-equilibrium concentrations; this method may improve alloy surface activation. Using Ti ion implantation, Kashkarov et al. [23] investigated the microstructure, defect structure, and hydrogen trapping in zirconium alloy Zr–1Nb. The results showed that the concentration of vacancy-type defects was rising with increasing bias voltage, which led to the strong interaction of hydrogen with vacancy-type defects. Suda et al. [22] investigated the effect of argon ion implantation surface modification on the hydrogenation property of Ti–Fe alloy. They observed significant improvement in initial activation properties, resulting in a significantly improved initial hydrogenation process of Ti–Fe alloy at 373 K and 1 MPa. Various reports have also corroborated such observations leading to increased hydrogen storage capacity. However, other reports show rather a decrease in hydrogen uptake [27–31].

Pd(10 nm)/Ti(50 nm)/Pd(10 nm)/Zr(50 nm)/Pd(10 nm) multi-layered stacks film deposited on Ti and Ti$_6$Al$_4$V alloy substrates were implanted with 150 keV argon ions at room temperature at a fluence ranging from 1×10^{12} ion/cm^2-1×10^{16} ion/cm^2, in this investigation. The samples were annealed at the same hydrogenation temperature of 550 °C under two ambient conditions: low pressure (3×10^{-3} Torr) and pure H$_2$ gases. Magogodi et al. [28] used this temperature to anneal Pd/Ti/Pd multilayer stack films in pure H$_2$ and discovered that the structural integrity was preserved with the formation of the TiH$_2$ phase, which indicates hydrogen absorption. Maebela et al. [32] studied the stability of the multilayer stack system at 550 °C, the results indicated no intermixing suggesting that the system was stable up to 500 °C in an H$_2$ environment. The main aim of this study is to probe the integrity of the layers upon annealing. The characterization techniques for both systems include the conventional Rutherford backscattering (RBS) technique to study any possible interfacial, diffusion, of atoms, elastic recoil detection analysis (ERDA) for the profiling of H in the samples, X-ray diffraction (XRD) to study the phase formation while scanning electron microscopy (SEM) was used to study the surface morphology.

2. Materials and experimental methods

The multilayer film stack of Ti (99.999 %), Pd (99.999 %), and Zr (99.999 %) metal targets were prepared sequentially on Ti and Ti$_6$Al$_4$V alloy substrates using the electron beam evaporator at iThemba laboratories for accelerator-based sciences (iThemba LABS) in Cape Town. Before depositions, Ti and Ti$_6$Al$_4$V alloy substrates were ultrasonically cleaned sequentially using acetone and methanol for 20 min. Substrates were mounted on a non-rotating substrate holder and transferred into the chamber. The targets were placed in three separate crucibles inside the chamber, creating a vacuum of 1×10^{-7} Torr. Depending on the material, the sequential deposition of Pd/Zr/Pd/Ti/Pd multilayer stack films was achieved using the emission current between 37.6 and 67 mA, and the deposition rate was maintained between 0.04 and 0.66 Å/s. The deposition chamber pressure was maintained at about 3×10^{-7} Torr during the deposition and the thickness was monitored using a thickness crystal monitor. Selected samples were implanted with 150 keV Ar ions at room temperature using the variation-Extrion 200-20A2F model ion implanter with an ES-30/25C processing station at iThemba labs in Johannesburg. The implanted samples were then annealed for 1 h at 550 °C in the pure H$_2$ gas environment and chamber pressure of 2.8×10^{-3} Torr. The H$_2$ gas flow rate was kept at 20 SCCM, which is the maximum sputtering gas flow rate.

The interfacial intermixing between the layers was investigated using the RBS technique using a near oxygen resonance energy of 3.45 MeV He^{++} ions from a 3 MV Tandetron accelerator, at iThemba LABS. The experimental data was collected at a 165° backscattering angle, using a surface barrier detector (with 20 keV resolution), with the chamber evacuated to 5×10^{-6} mbar vacuum

pressure. The sample surface was tilted by 5° towards the detector and the beam spot size was fixed to 2 mm. The channel positions were calibrated using a standard sample of AuCo/SiO2/Si (gold-cobalt on top of Si dioxide, deposited on the Si substrate). Furthermore, 3 MeV He^{++} beam energy was used to investigate the depth profile and the presence of hydrogen atoms in the samples via the conventional ERDA technique. For every analysed sample, a total collected charge of 40 μC and an average current of ~ 60 nA were maintained for both RBS and ERDA. A silicon (Si) particle detector with an energy resolution of about 23 keV, positioned at a 30° recoil angle, was used to record the energy spectra for the recoiled hydrogen atoms. The detector's resolution determines the energy resolution of ERDA, which is influenced by the energy straggling in the He^{++} stopping foil. This results in a value of ~23 keV and a concentration detection limit of 0.1 at.% [23]. To prevent charging effects, the 15 μm thick Kapton standard was coated with a 1 nm platinum layer before being used for channel positions and energy calibration. RBS and ERDA spectra were simulated using SIMNRA software, version 7.03 [https://mam.home.ipp.mpg.de], with the SigmaCalc 2.0, allowing calculations for cross-section data for the non-Rutherford scattering and nuclear reactions for many ion-target combinations at any angle. The simulation allowed the calculation of the composition and thickness of the multilayer stack system from RBS data. The compound formation and their related phases between the deposited layers were studied using the D8 Advance Bruker XRD diffractometer equipped with copper X-ray source (Cu-Kα radiation, λ ≈ 1.54 Å). X'pert highscore plus search and match software was used to identify peaks and associated crystal phases. The collected data was compared to the reference diffraction patterns present in the International Centre for Diffraction Data (ICDD). The surface microstructural changes for as-deposited and 150 keV implanted samples were studied using a scanning electron microscope (SEM). SEM images for the multilayer stack system were acquired using Zeiss Auriga field emission gun SEM (FEG-SEM) operated at 5 keV beam energy. Below is the experimental flow chart, showing the summary of sample preparation, ion implantation, sample annealing, and characterisation techniques (Fig. 1).

3. Results and discussion

3.1. SRIM simulation

The Stopping and Range of Ions in Matter (SRIM) simulation code is widely used to calculate a variety of parameters related to ion beam implantation and ion beam processing materials [22]. The core program of SRIM is TRIM (transport of ions in matter), which is based on a numerical method known as Monte Carlo simulation. The SRIM is a software package that computes particle radiation damage (known as atomic displacements per atom (dpa)) based on the stopping and range of ions in the target material. It calculates the motion of each ion as well as the interaction of each ion with matter, and the outputs are ion distribution, ion/recoil, energy loss, damage event, and ion stopping range/power. In this study, the calculations were done using 10,000 incident ions for statistical purposes with an option "Detailed Calculation with full Damage Cascades" to follow all incident ions. The threshold displacement energies of 30, 42, and 40 eV for Ti, Pd, and Zr were employed, with zero lattice binding energies, as determined by Konobeyev et al. [31].

Fig. 2(a–d) shows SRIM simulation of (a) ion/recoil distribution (X–Y plane) and (b) the ion penetration range (88.5 nm) of 150 keV argon ion penetrating Pd/Zr/Pd/Ti/Pd multilayer film stack on Ti from a perpendicular direction, (c) target vacancies created, and (d) the collision processes. According to the SRIM simulation (Fig. 2), two collision processes, i.e., electronic, and nuclear collisions, occurred as 150 keV argon ions were impinging on multilayered film stacks and the substrates resulting in energy loss, Fig. 2(d), in these two processes (electronic and nuclear) until the ions come to rest in the Ti and Ti_6Al_4V alloy substrates. According to the literature [33,34], the nuclear collision processes contribute to radiation damage such as defects and ion tracks. The maximum nuclear energy loss value obtained was about 90 eV/nm and much higher than that of the electronic energy loss which was less than 10 eV/nm.
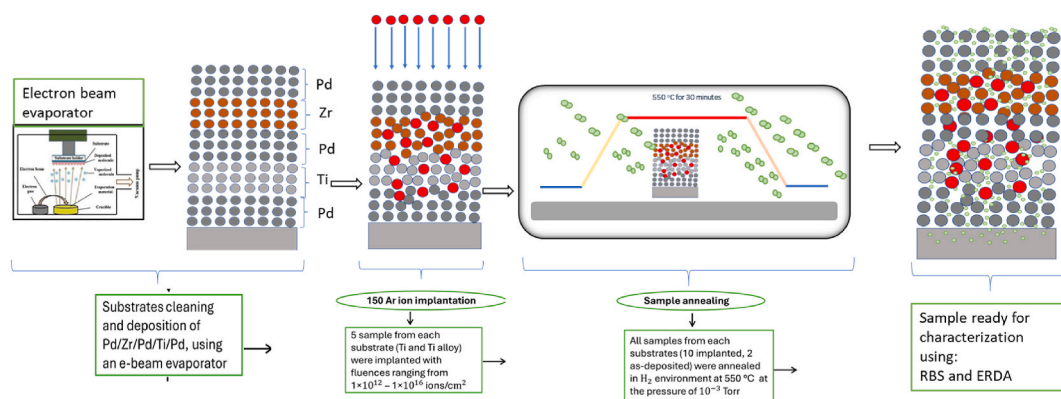

Fig. 1. The experimental flow chart summarizing sample preparation, 150 argon ion implantation, sample annealing, and characterisation procedures.
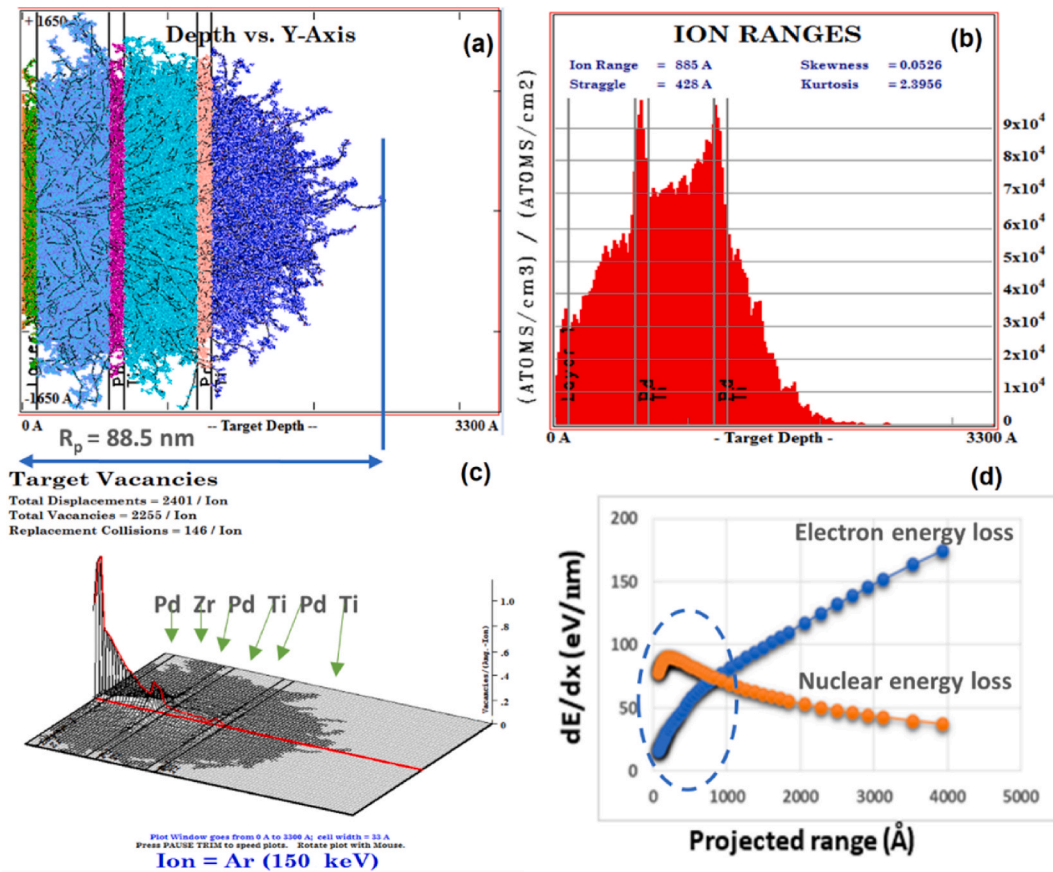
Fig. 2. SRIM simulation of (a) ion/recoil distribution and (b) the ion penetration range (88.5 nm) of 150 keV argon ion penetrating Pd/Zr/Pd/Ti/Pd multilayer film stack on Ti from a perpendicular direction, (c) target vacancies created, and (d) the collision processes.
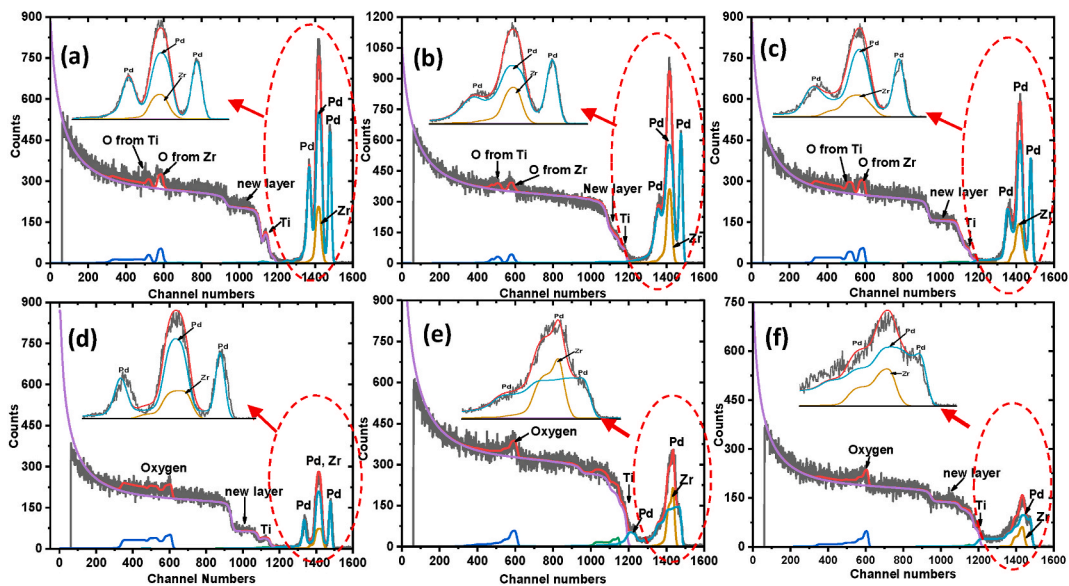

Fig. 3. (a) RBS spectra of as-deposited Pd/Zr/Pd/Ti/Pd multilayer film stack on Ti, (b–f) show spectra of 150 keV Ar ion-implanted samples at a fluence of 1×10^{12} ion/cm^2, 1×10^{13} ion/cm^2, 1×10^{14} ion/cm^2, 1×10^{15} ion/cm^2, and 1×10^{16} ion/cm^2 respectively after annealing at 550 °C in pure H$_2$ environment.

3.2. Rutherford backscattering spectroscopy

Fig. 3 (a) shows the RBS spectrum of as-deposited Pd/Ti/Pd/Zr/Pd multilayer film stack on Ti while Fig. 3(b–f) show spectra of 150 keV Ar ion-implanted samples at a fluence of 1×10^{12} ion/cm^2, 1×10^{13} ion/cm^2, 1×10^{14} ion/cm^2, 1×10^{15} ion/cm^2, and 1×10^{16} ion/cm^2, respectively, as labelled after annealing at 550 °C in pure H$_2$ environment. In Fig. 3(a), the position of the elements in all layers can be identified, Pd surface layer appearing at ~1475, and the buried Pd layers appearing at lower channel positions at ~1430 and ~1355 due to the energy loss experienced by probing ions in Zr and Ti layers. Ti and Zr in the buried layers appeared at channel positions ~1140 and ~1430 respectively due to the energy loss of probing ions. The closeness of the kinematic factors for Pd and Zr in RBS measurement, also coupled with the energy loss, hindered a clear separation of these two elements hence an overlap of the Pd signal from the second layer and the Zr layer was observed. The oxygen (O) contamination was observed at channel positions ~515 and ~580. The Pd layers in Fig. 3(a) were simulated without any inclusion of contamination and their thicknesses were found to be 138×10^{15} atoms/cm^2 (surface layer), 235×10^{15} atoms/cm^2 (middle layer), and 128×10^{15} atoms/cm^2 (bottom layer). The Ti and Zr layers in Fig. 3(a) could only be simulated with the inclusion of O contamination and their thicknesses were found to be 790×10^{15} atoms/cm^2 (Ti layer), and 831×10^{15} atoms/cm^2 (Zr layer). As we have previously reported, the presence of O in the Zr and Ti layers cannot be avoided at a working pressure of 6×10^{-7} Torr [9], and a similar preparation method condition was followed in this investigation.

The best simulation could only be achieved with stoichiometries 70 at% Zr and 30 at% O for the Zr–O layer, and 30 at% Ti and 70 at% O for the Ti–O layer.

For thermally annealed implanted samples, Fig. 3(b–f), the following changes were observed.

i. Fig. 3(b), at a fluence of 1×10^{12} atoms/cm^2, the thermal instability of the system was observed following the consumption of the second and third Pd layers. As a result, a drop in intensity of the two layers occurred in comparison to the Pd layers of the non-annealed samples. In this process, a Ti–O–Pd layer is formed. The observed new layer was simulated with compositions of 45 at% O, 44 at% Ti, 1 at% Ar, and 10 at% Pd stoichiometry, with a thickness of 206×10^{15} atoms/cm^2. This indicated the inter-diffusion of Pd atoms into the Ti–O layer.

ii. Fig. 3(c–d), at a fluence of 1×10^{13} atoms/cm^2 and 1×10^{14} atoms/cm^2, the thermal instability of the system continued accompanied by a further consumption and drop in intensity of the two Pd layers. This leads to an increase in the thickness of the newly formed Ti–O–Pd layer. The simulation of this layer gives elemental compositions of 75.4351 at% O, 23.8010 at% Ti, and 0.535149 at% Pd and 0.00228790 at% Ar stoichiometry with a thickness of 3473×10^{15} atoms/cm^2. These results suggest that the diffusion of Pd atoms into the Ti–O layer and the substrate took place.

iii. Fig. 3(e–f), at a fluence of 1×10^{15} atoms/cm^2 and 1×10^{16} atoms/cm^2, the consumption of all Pd layers was observed and reached a level such that individual layers became one layer that could not be resolved, indicating a complete intermixing of layers. The simulation was achieved by varying the composition of elements over multiple layers with varying thicknesses, with Ti–O being the dominant phase diffusing toward the surface.

The same trend observed in samples deposited on Ti substrate, Fig. 3(a), was observed in multilayers deposited in Ti$_6$Al$_4$V alloy. In Fig. 4(a) the position of the elements in all layers can be identified, Pd surface layer appearing at 1475, and the buried Pd layers

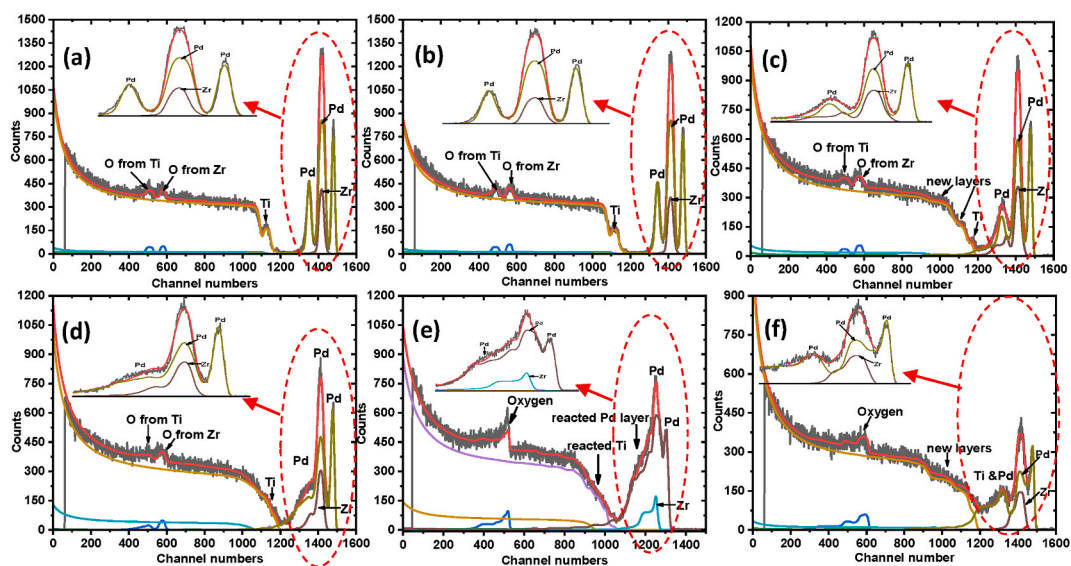**Fig. 4.** (a) RBS spectra of as-deposited Pd/Ti/Pd/Zr/Pd multilayer film stack on Ti$_6$Al$_4$V alloy, (b–f) show spectra of 150 keV Ar ion implanted samples at a fluence from 1×10^{12} ion/cm^2-1×10^{16} ion/cm^2 respectively after annealing at 550 °C in pure H$_2$ environment.

appearing at lower channel positions (1430 and 1355) due to the energy loss experienced by probing ions in Zr and Ti layers at channel positions 1140 and 1130 respectively. The oxygen (O) contamination was observed at channel positions 515 and 580. The Pd layers in Fig. 4(a) were simulated without any inclusion of contamination and their thicknesses were found to be 172×10^{15} atoms/cm^2 (surface layer), 247×10^{15} atoms/cm^2 (middle layer), and 141×10^{15} atoms/cm^2 (bottom layer). The Ti and Zr layers in Fig. 4(a) could only be simulated with the inclusion of O contamination and their thicknesses were found to be 1141×10^{15} atoms/cm^2 (Ti layer), and 647×10^{15} atoms/cm^2 (Zr layer), simulated with 57 at% Zr and 43 at% O, 32 at% Ti and 68 at % O stoichiometry.

i. Fig. 4(b–c), at a fluence of 1×10^{12} atoms/cm^2 and 1×10^{13} atoms/cm^2, the thermal instability of the system was observed due to the consumption of only the third Pd layer as evidenced by a continuous drop of the peak intensities, accompanied by the continual increase in thickness of the newly formed Ti–O–Pd layer. This indicated the diffusion of Pd atoms into the Ti–O layer.

ii. Fig. 4(d–f), at a fluence of 1×10^{14} atoms/cm^2, 1×10^{15} atoms/cm^2, 1×10^{16} atoms/cm^2, the consumption of all layers was observed. However, individual layers could still be identified and resolved, indicating incomplete layers intermixing. The simulation was achieved by varying the composition of elements over multiple layers with varying thicknesses. Ti–O is the dominant phase diffusing toward the surface as shown in the profile in Fig. 4(a–c).

The elemental concentration profile plots for as-deposited sample on Ti substrate (Fig. 5(a)) and 150 keV Ar ion-implanted samples at a fluence of 1×10^{16} ion/cm^2 on Ti and Ti$_6$Al$_4$V substrates respectively after annealing at 550 °C in pure H$_2$ are shown (Fig. 5(b–c)). SIMRA simulations were used to determine the stoichiometry depicted in Fig. 5. The elemental concentration profiles were directly extracted from the fitted spectra in Figs. 3 and 4. This was done for the (a) as-deposited sample, and for the 150 keV Ar ion implanted samples at a fluence of 1×10^{16} ion/cm^2 on Ti and Ti$_6$Al$_4$V substrates, after annealing at 550 °C in a pure H$_2$ environment. The obtained ratio was then converted into percentages and plotted as shown in Fig. 5. The results show that the reaction starts with the Pd layer in contact with the substrates reacting with Ti atoms of the substrate. In contrast, the other layers remain intact, especially at 1×10^{12} ions/cm^2. As the fluence increases, all other layers begin to follow and participate in the reaction-forming phases as shown in Fig. 5(b) and (c). At the highest fluence, that is, 1×10^{16} ions/cm^2, all the layers experience the intermixing reaction that evolves toward completion as seen by the convolution of all layers. An out-diffusion of Ar ions toward the surface was also observed and increased as the implantation fluence was increased.

It is worth noting that the layer intermixing started in the buried layers migrating toward the surface layer. The buried layers are in the Ar ion depth range (see Fig. 2(a)), and they contain a high number of the implanted Ar ions, which weakened these layers. It has
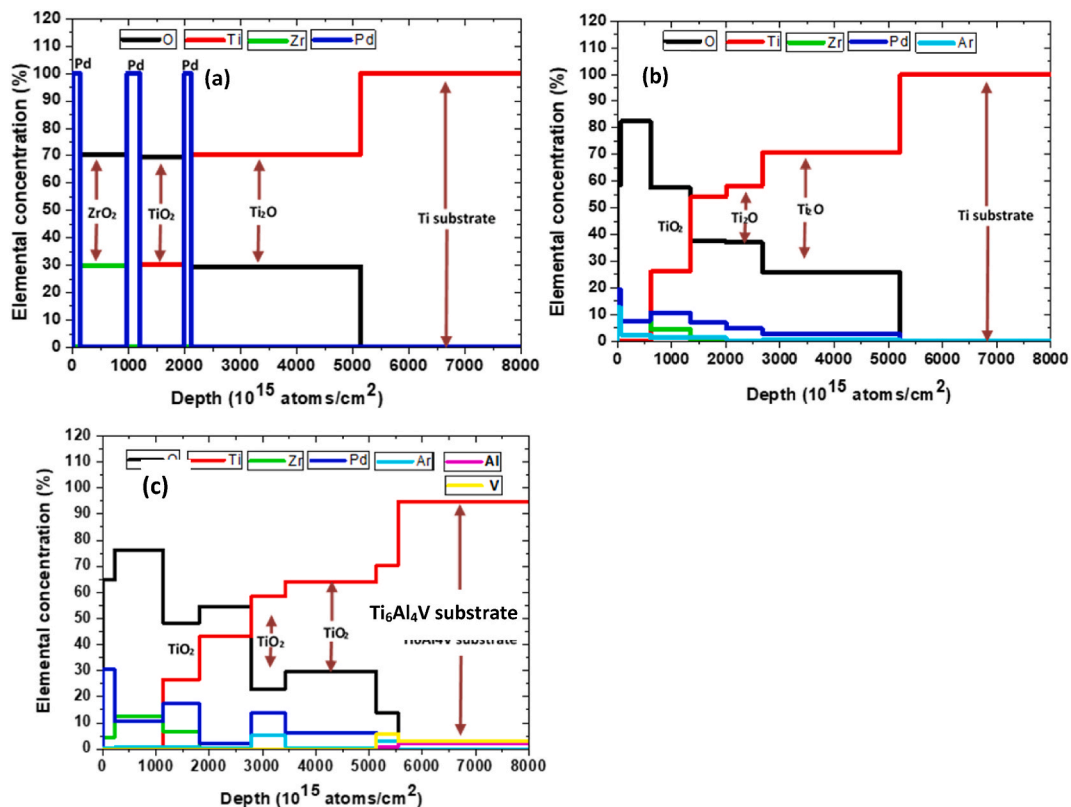

Fig. 5. Elemental concentration profiles, (a) as-deposited sample, (b and c) 150 keV Ar ion implanted samples at a fluence of 1×10^{16} ion/cm^2 on Ti and Ti$_6$Al$_4$V substrates respectively after annealing at 550 °C in pure H$_2$ environment.

been reported in the literature that some ion-implanted systems become unstable due to latent oxide damage during ion implantation and a conducting film or substrate can eliminate this effect and prevent instability [35,36]. Also, the implantation of Ar ions leads to the relaxation of the system and a more homogeneous distribution of bond energy in individual layers, especially of superlattice. The point defects during implantation activate the dislocation nucleation process in the layer interface, reducing the compressive stresses [35,36]. It is common knowledge that when Ti and its alloys are exposed to air or water, a native titanium oxide layer is spontaneously formed. Our substrates (Ti and Ti_6Al_4V) as well as the Ti target had that native oxide layer before they were loaded into the vacuum chamber. The zirconium might also have an oxide layer before it was loaded as it is also a highly reactive element. The vacuum chamber contamination is the second source of the oxygen signal under a working pressure of 6×10^{-7} Torr, oxygen contamination is inevitable [9]. It is worth mentioning that the RBS technique is more sensitive to heavy elements as the cross-section of elastic scattering is proportional to the square of the atomic number. However, when the energy of alpha particles is increased, the sensitivity for light elements, such as oxygen, can be substantially increased by a large enhancement of the elastic cross-section. In our investigation, the use of a near-oxygen resonance of 3.45 MeV alpha particles allows us to observe the oxygen signal. If the standard RBS (2 MeV alpha particles) were performed, the oxygen signal would not be observed.

3.3. X-ray diffraction

Fig. 6(a) shows XRD spectra of as-deposited multilayer stack on pure Ti substrate as well as of 150 keV Ar ion-implanted samples at fluences in the range 1×10^{12} ion/cm^2-1×10^{16} ions/cm^2 after annealing at 550 °C in pure H$_2$ environment. Fig. 6(b) displays equivalent spectra in the same sequence but with Ti$_6$Al$_4$V substrate. In both figures, the X-ray diffraction patterns of both substrates displayed peaks corresponding to the hexagonal α-Ti phase but a new peak corresponding to the cubic β-Ti phase appeared in the pattern of the Ti alloy substrate only. The as-deposited samples on both substrates showed additional diffraction peaks corresponding to the simple cubic (SC) Pd phase. Meanwhile, after implantation and annealing, the diffraction patterns showed peaks corresponding to the face-centered cubic (FCC) Pd$_{1.5}$H$_2$, hexagonal α-Ti phase, and the body-centered cubic (BCC) PdTi$_2$, indicating intermixing of films as a result of thermal annealing. Furthermore, TiH$_2$ and ZrH$_2$ hydrides crystallizing in the face-centered tetragonal (FCT) were observed. As indicated in Table 1, other additional phases were observed due to elemental interfacial diffusion of Pd layers.

Furthermore, some of the indices of crystal faces shown in Fig. 6 overlap with other crystal structure phases observed. Hydrogen molecules were observed corresponding to the crystal index of (101), which shows that hydrogen is bonded chemically and found in the crakes due to ion implantation. The second peak shows the overlapping of (111), (002), and (200) crystal planes which correspond to TiH, ZrH, and ZrH$_2$ respectively. In the third and fourth peak crystal planes of (200), (002), and (102) corresponding to TiH$_2$, TiH, H$_2$, and ZrH$_2$ were observed. The fifth peak only shows a (101) plane corresponding to the Pd$_{1.5}$H$_2$ compound. The (002) corresponds to TiH$_2$, the (200) crystal plane corresponds to Pd, and the (202) plane corresponds to ZrH, in peaks sixth, seventh, and ninth respectively. In the eighth peak, two overlapping crystal planes (220) and (112) were observed corresponding to ZrH$_2$ and TiH$_2$. The tenth peak and eleventh peak showed crystal planes (201), (212), (202), and (200) corresponding to H$_2$, ZrH$_2$, and Pd$_{1.5}$H$_2$. The twelfth peaks have three overlapping crystal planes (113) corresponding to TiH and ZrH$_2$, however, the other crystal plane (222) corresponds
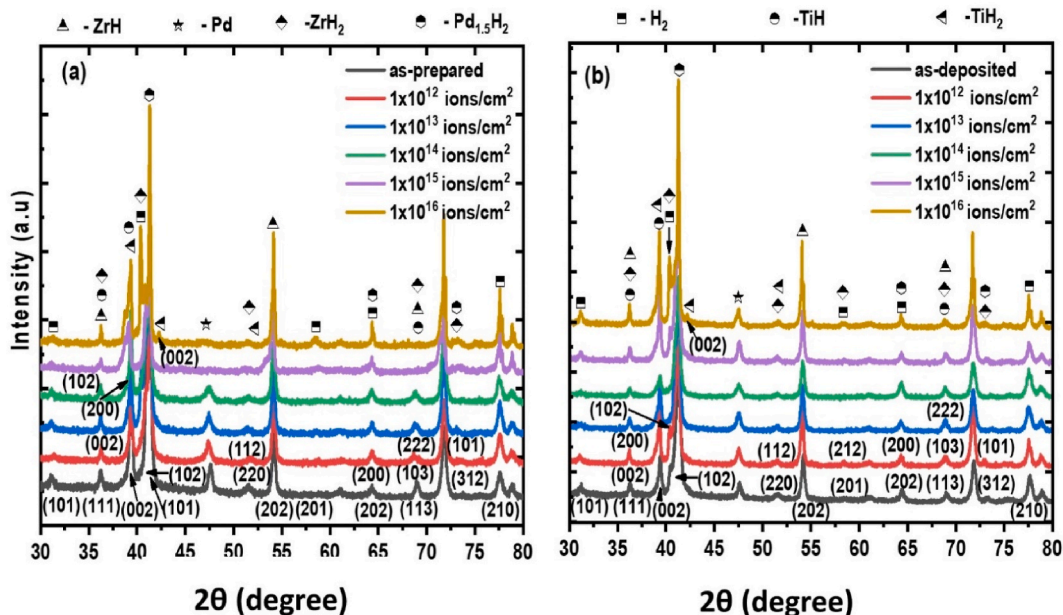

Fig. 6. XRD spectra of as-deposited Pd/Ti/Pd/Zr/Pd multilayer film stack on (a) Ti substrate and (b) Ti$_6$Al$_4$V alloy substrate, showing the spectra of 150 keV Ar ion implanted samples at fluences in the range 1×10^{12} ion/cm^2-1×10^{16} ion/cm^2 after annealing at 550 °C in pure H$_2$ environment.

Table 1
Crystallographic information of different phases as observed in both substrates.

Phase	Pattern no.	Space group	Lattice parameters (Å)
Hexagonal α-Ti	01-089-3726	$P6_3/mmc$ (194)	a = b = 2.95 nm; c = 4.69 nm
Cubic β-Ti	01-089-3073	$Im\text{-}3m$ (229)	a = b = c = 3.31 nm
Hexagonal α-Zr	00-005-0665	$P6_3/mmc$ (194)	a = b = 3.23 nm; c = 5.15 nm
Cubic β-Zr	01-089-4916	$Im\text{-}3m$ (225)	a = b = c = 3.62 nm
Cubic Pd	01-089-4897	$Fm\text{-}3m$ (225)	a = b = c = 3.89 nm
Hexagonal $TiPd_3$	00-035-1361	$P6_3/mmc$ (194)	a = b = 5.49; c = 8.96 nm
Tetragonal TiH	00-040-1244	$P4_2/ncm$(138)	a = b = 4.20 nm; 4.58 nm
Tetragonal TiH_2	03-065-6949	$12/mmm$(139)	a = b = 4.53 nm; c = 4.28 nm
Tetragonal ZrH	00-034-0690	$P4_2/n$ (86)	a = b = 4.60 nm; c = 4.97 nm
Tetragonal ZrH_2	00-020-1465	$12/mmm$(139)	a = b = 4.97 nm; c = 4.46 nm

to ZrH. The fourteenth peaks have two overlapping planes (312) and (101) corresponding to ZrH_2 and $Pd_{1.5}H_2$, respectively. Finally, the (210) crystal plane corresponding to H_2 was observed.

3.4. Microstructural analysis

Fig. 7 shows the surface morphology of (a) as-deposited samples, (b-f) 150 keV Ar ion implanted samples at fluences ranging from 1×10^{12} ion/cm²-1×10^{16} ion/cm² after annealing at 550 °C in pure H_2 environment, on Ti substrate. The as-deposited samples showed a homogeneous surface while a smooth surface with cracks and granular crystals formed was observed on annealed samples as shown in Fig. 7(b). As shown in Figs, the granular structure increased with increasing fluence, resulting in larger coalesced multi-faceted crystals. 7(c-e), as it was observed in the XRD results, and the diffusion of atoms was also observed in the RBS results. At fluence of 1×10^{16} ion/cm², the surface became relatively smooth surface with cracked and peeled regions.

The trend observed in as-deposited samples on Ti substrate, Fig. 7(a), was also observed in as-deposited samples on Ti_6Al_4V substrate (Fig. 8(a)). However, the as-deposited samples in Fig. 8(a) displayed relatively smooth surfaces with some cracks that developed during deposition. With 150 keV Ar ion implantation at fluences ranging from 1×10^{12} ion/cm²-1×10^{16} ion/cm² (Fig. 8 (b–f)), after annealing at 550 °C in pure H_2 environment, irregular structures on the surface began to develop and grew with increasing fluence to the point of melting as can be seen in Fig. 8(f). This is an indication of a very unstable system as a direct influence of implanted ions, with the evidence of intermixing of layers (diffusion of atoms) as observed in the RBS with the intensity changes of the
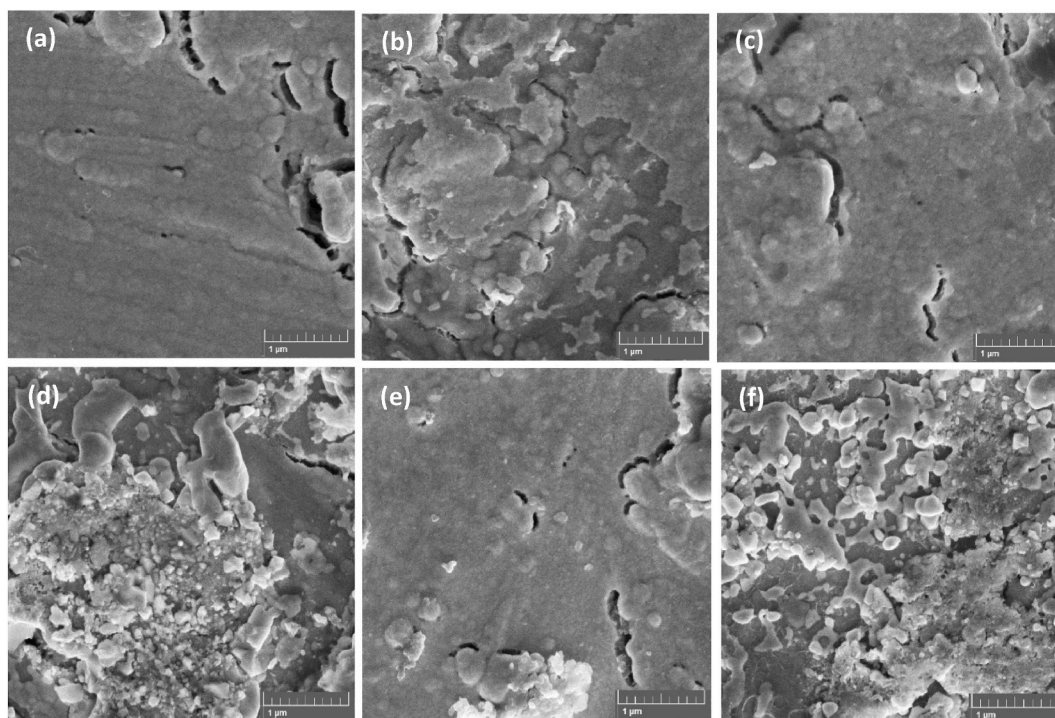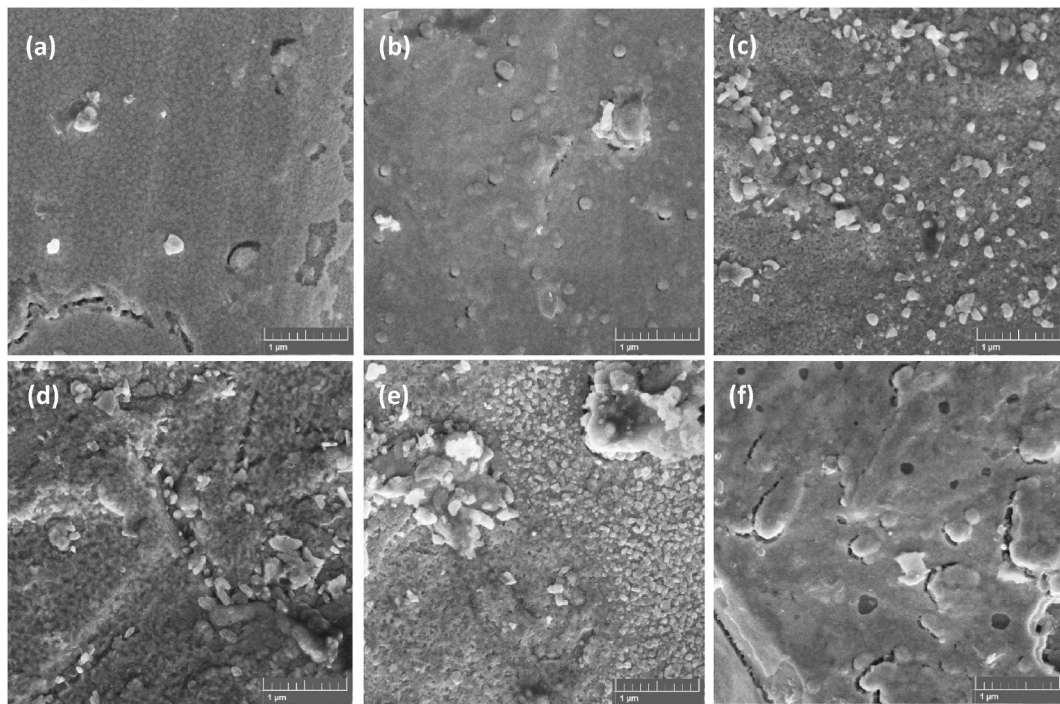

Fig. 7. SEM images of (a) as-deposited Pd/Ti/Pd/Zr/Pd multilayer film stack on Ti substrates, (b–f) 150 keV Ar ion implanted samples at a fluence ranging from 1×10^{12} ion/cm²-1×10^{16} ion/cm² after annealing at 550 °C in pure H_2 environment.

Fig. 8. SEM images of (a) as-deposited Pd/Ti/Pd/Zr/Pd multilayer film stack on Ti$_6$Al$_4$V substrate, (b–f) 150 keV Ar ion implanted samples at a fluence ranging from 1×10^{12} ion/cm^2-1×10^{16} ion/cm^2 after annealing at 550 °C in pure H$_2$ environment.

other layers and with multiple phases observed in the XRD results.

3.5. Elastic recoil detection analysis (ERDA)

Fig. 9(a) shows ERDA spectra of a deposited multilayer stack on pure Ti substrate as well as of 150 keV Ar ion implanted samples at a fluence of 1×10^{12} ion/cm^2, 1×10^{13} ion/cm^2, 1×10^{14} ion/cm^2, 1×10^{15} ion/cm^2, and 1×10^{16} ion/cm^2 respectively after annealing at 550 °C in pure H$_2$ environment. Fig. 9(b) displays equivalent spectra in the same sequence with Ti$_6$Al$_4$V substrate. In both Fig. 9(a–b), ERDA spectra show that a significant amount of surface H component was detected and dropped towards the bulk of the samples. Only surface H components exist in the deposited sample due to the atmosphere's hydrocarbons. Fig. 9(c–d) shows the corresponding depth profile of spectra in Fig. 9(a–b). The H amount absorbed by the system during annealing in the H$_2$ environment is presented in Table 2.

4. Conclusion

We have investigated the structural stability of implanted Pd/Zr/Pd/Ti/Pd multilayer stack in a hydrogen annealing environment. The samples were implanted with 150 keV argon ions at fluences in the range 1×10^{12}–1×10^{16} ion/cm^2 at room temperature and subsequently annealed at 550 °C for an hour in the pure H$_2$ gas environment, with a gas flow rate kept at 20 SCCM. The RBS analysis of the samples revealed instability of the layers that is increasing with the implantation fluence. In both multilayers on Ti and Ti$_6$Al$_4$V alloy substrates, it was observed that as the implantation fluence increased, the thermal instability of the system increased. However, in the multilayers deposited on the Ti$_6$Al$_4$V substrate at all fluences, the individual layers could still be identified and resolved, showing incomplete layers intermixing. This exacerbated the consumption of the layers as evidenced by the continuous dropping of their peak intensity. During this process, a continual increase in the thickness of the newly formed Ti–O–Pd layer was observed. The XRD analysis indicated the formation of multiple phases as the implantation fluence increased. New crystal phases such as such as Pd$_3$Ti, ZrH$_2$, and TiH$_2$ were formed. Hydrogen profiling data was collected using the ERDA technique. The hydrogen was absorbed within the ion track but decreased towards the bulk of the Ti and Ti$_6$Al$_4$V substrates. This observation indicated that the application of this multilayer stacked system cannot be applied in an environment beyond 350 °C when argon ions are implanted.

Limitations

The limitations were the characterization tools and the implantation ions; some of the ions we planned to employ were unavailable due to the ion implanter's restrictions. The results revealed that the practical application of Pd/Zr/Pd/Ti/Pd multilayer stack film in
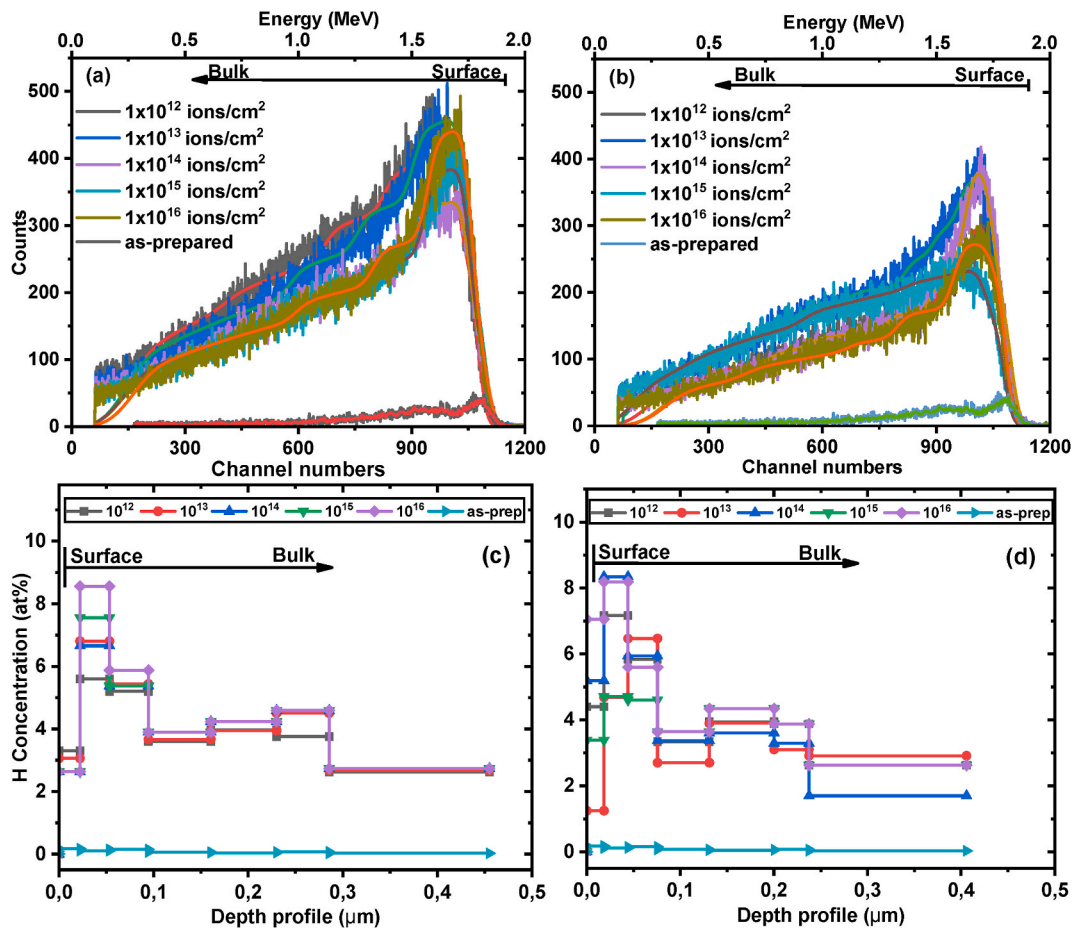
Fig. 9. ERDA spectra of Pd/Ti/Pd/Zr/Pd multilayer film stack on (a) Ti substrate and (b) Ti$_6$Al$_4$V alloy substrate, plot show spectra as-deposited and 150 keV Ar ion implanted samples at fluences ranging from 1×10^{12} ion/cm^2-1×10^{16} ion/cm^2, after annealing at 550 °C in pure H$_2$ environment. Fig. 9(c–d) shows the depth profiles for both substrates.

Table 2
Average H concentration over total probed depth.

Fluences (ions/cm^2)	Ti substrate	Ti$_6$Al$_4$V substrate
	Average H concentration (at%)	Average H concentration (at%)
As deposited	1.20	1.10
1×10^{12}	4.01	3.57
1×10^{13}	4.30	3.88
1×10^{14}	4.30	4.49
1×10^{15}	4.43	4.46
1×10^{16}	5.20	5.05

hydrogen application is limited to temperature, pressure, and the fluences of the 150 keV Ar ion implantation.

Data availability

Data will be made available on request.

CRediT authorship contribution statement

C.T. Thethwayo: Writing – review & editing, Writing – original draft, Visualization, Resources, Methodology, Investigation, Funding acquisition, Formal analysis, Data curation, Conceptualization. **C.B. Mtshali:** Writing – review & editing, Writing – original draft, Visualization, Supervision, Resources, Methodology, Formal analysis, Data curation, Conceptualization. **Z.M. Khumalo:** Writing

– review & editing, Visualization, Resources, Investigation, Data curation, Conceptualization. **K. Segola:** Writing – review & editing. **S. Nsengiyumva:** Writing – review & editing. **N. Mongwaketsi:** Writing – review & editing. **C.L. Ndlangamandla:** Writing – review & editing, Supervision. **P.N. Biyela:** Writing – review & editing.

Declaration of competing interest

Dear Editor, Authors declare that this work is not a duplicate of any study conducted before nor any part of the work published or submitted in any journal. The authors declare that they have no conflict of interest in the publication of this article.

Acknowledgments

References

[1] J. Tang, S. Wu, N. AlMasoud, T.S. Alomar, P. Wasnik, H. Li, Z.M. El-Bahy, J. Ren, X. Li, P. Zhang, Defect passivation in perovskite films by p-methoxy phenylacetonitrile for improved device efficiency and stability, Adv. Compos. Hybrid Mater. 6 (2023) 1551–1558, https://doi.org/10.1007/s42114-023-00732-2.

[2] X.-S. Xing, X. Zeng, Z. Zhou, Z.M. El-Bahy, M.H. Helal, Q. Gao, H. Algadi, P. Song, X. Liu, X. Zhang, Constructing iron-group doped metal–organic framework films on hematite photoanodes for efficient solar water splitting, Adv. Compos. Hybrid Mater. 6 (2023) 1941–19411, https://doi.org/10.1007/s42114-023-00777-3.

[3] Z. Zhuang, Z. Li, G. Gong, Q. Li, Y. Zhang, C. Huang, Y. Huang, L. Tian, P. Wang, Z. Guo, Two-dimensional superlattice films of gold nanoparticle-polystyrene composites: a bioactive platform for bone homeostasis maintenance, Adv. Compos. Hybrid Mater. 6 (2023) 1661–16615, https://doi.org/10.1007/s42114-023-00738-w.

[4] I.D. Wijayanti, R. Denys, Suwarno, A.A. Volodin, M.V. Lototskyy, M.N. Guzik, J. Nei, K. Young, H. Jørgen Roven, V. Yartys, Hydrides of Laves type Ti-Zr alloys with enhanced H storage capacity advanced metal hydride battery anodes, J. Alloys Compd. 828 (2020) 154–354, https://doi.org/10.1016/j.jallcom.2020.154354.

[5] K. Otsuka, X. Ren, Recent developments in the research of shape memory alloys, Intermetallics 7 (1999) 511–528, https://doi.org/10.1016/S0966-9795(98)00070-3.

[6] B.G. Priyadarshini, S. Aich, M. Chakraborty, Nano-crystalline NiTi alloy thin films fabricated using magnetron co-sputtering from elemental targets: effect of substrate conditions, Thin Solid Films 616 (2016) 733–745, https://doi.org/10.1016/j.tsf.2016.09.034.

[7] Van Humbeeck, Non-medical applications of shape memory alloys, Mater. Sci. Eng. (1999) 134–148, https://doi.org/10.1016/S0921-5093(99)00293-2, 273-275.

[8] J.L. Ke, C.H. Huang, Y.H. Chen, W.Y. Tsai, T.Y. Wei, J.C. Huang, In vitro biocompatibility response of Ti–Zr–Si thin film metallic glasses, Appl. Surf. Sci. 322 (2014) 41–46, https://doi.org/10.1016/j.apsusc.2014.09.204.

[9] Z. Khumalo, C. Thethwayo, C. Mtshali, M. Msimanga, M. Madito, N. Numan, N. Mongwaketsi, C. Kotsedi, N. Kheswa, Interfacial reaction and phase formation in Pd/ZrO/Pd/TiO/Pd multilayer stack on silicon substrate: investigated by ion beam techniques, Vacuum 214 (2023) 112–204, https://doi.org/10.1016/j.vacuum.2023.112204.

[10] M.K. Jangid, S.S. Sharma, D. Mathur, Y.C. Sharma, Optical, electrical and structural study of Mg/Ti bilayer thin film for hydrogen storage applications, Mater. Lett. X 10 (2021), https://doi.org/10.1016/j.mlblux.2021.100076, 100-076.

[11] H. Liu, L. Tan, Y. Guo, P. Chen, S. Gao, Z. Su, W. Liu, J. Zhao, Fabrication and electrochemical hydrogen storage performance of Ti49Zr26Ni25 alloy covered with Cd/Pd core/shell particles, Int. J. Hydrogen Energy 44 (2019) 24800–24809, https://doi.org/10.1016/j.ijhydene.2019.07.094.

[12] A. Vaidyanathan, P. Mane, V. Wagh, B. Chakraborty, Computational design for enhanced hydrogen storage on the newly synthesized 2D polyaramid via titanium and zirconium decoration, ACS Appl. Mater. Interfaces 16 (2024) 8589–8602, https://doi.org/10.1021/acsami.3c14088.

[13] B. Ge, Y. Hu, H. Zhang, J. Xu, P. Zhang, Y. Yue, H. Zhu, S. Lin, P. Yuan, Zirconium promoter effect on catalytic activity of Pd based catalysts for heterogeneous hydrogenation of nitrile butadiene rubber, Appl. Surf. Sci. 539 (2021) 148–212, https://doi.org/10.1016/j.apsusc.2020.148212.

[14] J. Kim, P. Gibbons, K. Kelton, Hydrogenation of Pd-coated samples of the Ti–Zr-based icosahedral phase and related crystalline phases, J. Alloys Compd. 266 (1998) 311–317, https://doi.org/10.1016/S0925-8388(97)00474-X.

[15] K. Drogowska, S. Flege, C. Schmitt, D. Rogalla, H.-W. Becker, N.-T. Kim-Ngan, A. Brudnik, Z. Tarnawski, K. Zakrzewska, M. Marszałek, Hydrogen charging effects in Pd/Ti/TiO2/Ti thin films deposited on Si (111) studied by ion beam analysis methods, Adv. Mater. Sci. Eng. 2012 (2012) 269603, https://doi.org/10.1155/2012/269603.

[16] A. Pundt, R. Kirchheim, Hydrogen in metals: microstructural aspects, Annu. Rev. Mater. Res. 36 (2006) 555–608, https://doi.org/10.1146/annurev.matsci.36.090804.094451.

[17] Leng, Z. Yang, X. Tang, M.H. Helal, Y. Qu, P. Xie, Z.M. El-Bahy, S. Meng, M.M. Ibrahim, C. Yu, Progress in percolative composites with negative permittivity for applications in electromagnetic interference shielding and capacitors, Adv. Compos. Hybrid Mater. 6 (2023) 1951–19521, https://doi.org/10.1007/s42114-023-00778-2.

[18] K. Sun, P. Yang, Q. He, R. Fan, Z. Wang, J. Tian, X. Yang, W. Duan, X. Wu, Z. Wang, Synergistic effect of dielectric resonance and plasma oscillation on negative permittivity behavior in La1-xSrxMnO3 single-phase ceramic, Ceram. Int. 48 (2022) 8417–8422, https://doi.org/10.1016/j.ceramint.2021.12.049.

[19] H. Wu, Y. Zhong, Y. Tang, Y. Huang, G. Liu, W. Sun, P. Xie, D. Pan, C. Liu, Z. Guo, Precise regulation of weakly negative permittivity in CaCu3Ti4O12 metacomposites by synergistic effects of carbon nanotubes and graphene, Adv. Compos. Hybrid Mater. 5 (2021) 419–430, https://doi.org/10.1007/s42114-021-00378-y.

[20] G. Fan, Z. Wang, H. Ren, Y. Liu, R. Fan, Dielectric dispersion of copper/rutile cermets: dielectric resonance, relaxation, and plasma oscillation, Scripta Mater. 190 (2021) 1–6, https://doi.org/10.1016/j.scriptamat.2020.08.027.

[21] G. Fan, Z. Wang, K. Sun, Y. Liu, R. Fan, Doped ceramics of indium oxides for negative permittivity materials in MHz-kHz frequency regions, J. Mater. Sci. Technol. 61 (2021) 125–131, https://doi.org/10.1016/j.jmst.2020.06.013.

[22] T. Suda, M. Ohkawa, S. Sawada, S. Watanabe, S. Ohnuki, S. Nagata, Effect of surface modification by ion implantation on hydrogenation property of TiFe alloy, Mater. Trans. 43 (2002) 2703–2705. https://www.jstage.jst.go.jp/article/matertrans/43/11/43_11_2703/_pdf.

[23] E. Kashkarov, N. Nikitenkov, A. Sutygina, R. Laptev, Y. Bordulev, A. Obrosov, M.O. Liedke, A. Wagner, A. Zak, S. Weiβ, Microstructure, defect structure and hydrogen trapping in zirconium alloy Zr-1Nb treated by plasma immersion Ti ion implantation and deposition, J. Alloys Compd. 732 (2018) 80–87, https://doi.org/10.1016/j.jallcom.2017.10.151.

[24] M. Asad, M. Sana, Potential of titanium-based alloys in the biomedical sector and their surface modification techniques: a review, Proc. IME C J. Mech. Eng. Sci. 10 (2023) 1–30, https://doi.org/10.1177/09544062231164506.

[25] J. Bandoli Monteiro, P.H. Condé Oliveira Prado, G.R. Zucco, T.M. Bastos Campos, J.P. Barros Machado, V.J. Trava-Airoldi, R. Marques de Melo, High-translucency zirconia following chemical vapor deposition with SiH 4: evidence of surface modifications and improved bonding, J. Adhesive Dent. 25 (2023) 1–12, https://doi.org/10.3290/j.jad.b3801051.

[26] L. Liu, T. Li, Q. Ruan, D. Li, C. Huang, X. Zhang, Y. Ma, Y. Wu, Z. Wu, R.Y. Fu, Enhanced mechanical properties of CrN coatings by plasma immersion ion ion implantation and deposition, Ceram. Int. 49 (2023) 6713–6719, https://doi.org/10.1016/j.ceramint.2022.10.215.

[27] W. Jiang, Q.-f. Pan, X. Huang, G. Li, Y. Fang, H.-q. Kou, T. Tang, Effect of low concentration of impurity gases on the hydrogen absorption performance of uranium, Int. J. Hydrogen Energy 47 (2023) 777–780, https://doi.org/10.1016/j.ijhydene.2023.03.082.

[28] J. Khan, L. Han, Oxygen vacancy in TiO 2: production methods and properties, updates on titanium dioxide, IntechOpen 10.5772 (2023) 195–258. Available from: https://www.intechopen.com/chapters/86988.

[29] S. Magogodi, C. Mtshali, S. Halindintwali, Z. Khumalo, N. Mongwaketsi, K. Cloete, M. Madito, C. Pieters, A. Sook, E. Mc Donald, Effect of the annealing atmosphere on the layer interdiffusion in Pd/Ti/Pd multilayer stacks deposited on pure Ti and Ti-alloy substrates, Nucl. Instrum. Methods Phys. Res. Sect. B Beam Interact. Mater. Atoms 461 (2019) 37–43, https://doi.org/10.1016/j.nimb.2019.09.018.

[30] K. Seshan, Handbook of thin film deposition techniques principles, methods, equipment and applications, second edition, CRC Press, in: https://edisciplinas.usp.br/pluginfile.php/7455566/mod_resource/content/1/Handbook_of_Thin_Film_Deposition_Process.pdf, 2002.

[31] A.Y. Konobeyev, U. Fischer, Y.A. Korovin, S.P. Simakov, Evaluation of effective threshold displacement energies and other data required for the calculation of advanced atomic displacement cross-sections, Nuclear Energy and Technology 3 (2017) 169–175, https://doi.org/10.1016/j.nucet.2017.08.007.

[32] N.Y. Maebela, C. Mtshali, Z. Khumalo, R. Madjoe, C. Arendse, F. Cummings, M. Madito, N. Mongwaketsi, Influence of implanted 150 keV Fe ion and 100 keV Mg ions on hydrogen absorption by Pd/Ti/V/Pd/Ti multilayer films on Ti substrate, Nucl. Instrum. Methods Phys. Res. B 523 (2022) 1–7, https://doi.org/10.1016/j.nimb.2022.05.002.

[33] M.J. Madito, M.Y.A. Ismail, T.T. Hlatshwayo, C.B. Mtshali, The nature of surface defects in Xe ion-implanted glassy carbon annealed at high temperatures: Raman spectroscopy analysis, Appl. Surf. Sci. 506 (2020) 145001–145013, https://doi.org/10.1016/j.apsusc.2019.145001.

[34] M.J. Madito, T.T. Hlatshwayo, V.A. Skuratov, C.B. Mtshali, N. Manyala, Z.M. Khumalo, Characterization of 167 MeV Xe ion irradiated n-type 4H-SiC, Appl. Surf. Sci. 493 (2019) 1291–1298, https://doi.org/10.1016/j.apsusc.2019.07.147.

[35] O. Liubchenko, T. Sabov, V. Kladko V. Melnik, V. Yukhymchuk, B. Romanyuk, O. Kolomys, O. Hreshchuk, O. Dubikovskyi, Z. Maksimenko, O. Gudymenko, A. Belyaev, Modification of elastic deformations and analysis of structural and optical changes in Ar+-implanted AlN/GaN superlattices, Appl. Nanosci. 10 (2020) 2479–2487, https://doi.org/10.1007/s13204-019-01000-w.

[36] S. Tan, X. Deng, B. Zhang, J. Zhang, Thermal stability of F ion-implant isolated AlGaN/GaN heterostructures, Sci. China Phys. Mech. Astron. 61 (2018) 127311–127315, https://doi.org/10.1007/s11433-018-9312-7.